The IMA Volumes in Mathematics and its Applications

Volume 142

Series Editors
Douglas N. Arnold Arnd Scheel

Institute for Mathematics and its Applications (IMA)

The **Institute for Mathematics and its Applications** was established by a grant from the National Science Foundation to the University of Minnesota in 1982. The primary mission of the IMA is to foster research of a truly interdisciplinary nature, establishing links between mathematics of the highest caliber and important scientific and technological problems from other disciplines and industries. To this end, the IMA organizes a wide variety of programs, ranging from short intense workshops in areas of exceptional interest and opportunity to extensive thematic programs lasting a year. IMA Volumes are used to communicate results of these programs that we believe are of particular value to the broader scientific community.

The full list of IMA books can be found at the Web site of the Institute for Mathematics and its Applications:

http://www.ima.umn.edu/springer/volumes.html

Douglas N. Arnold, Director of the IMA

* * * * * * * * * *

IMA ANNUAL PROGRAMS

1982–1983	Statistical and Continuum Approaches to Phase Transition
1983–1984	Mathematical Models for the Economics of Decentralized Resource Allocation
1984–1985	Continuum Physics and Partial Differential Equations
1985–1986	Stochastic Differential Equations and Their Applications
1986–1987	Scientific Computation
1987–1988	Applied Combinatorics
1988–1989	Nonlinear Waves
1989–1990	Dynamical Systems and Their Applications
1990–1991	Phase Transitions and Free Boundaries
1991–1992	Applied Linear Algebra
1992–1993	Control Theory and its Applications
1993–1994	Emerging Applications of Probability
1994–1995	Waves and Scattering
1995–1996	Mathematical Methods in Material Science
1996–1997	Mathematics of High Performance Computing
1997–1998	Emerging Applications of Dynamical Systems
1998–1999	Mathematics in Biology

Continued at the back

Douglas N. Arnold Pavel B. Bochev
Richard B. Lehoucq Roy A. Nicolaides
Mikhail Shashkov
Editors

Compatible Spatial Discretizations

Springer

Douglas N. Arnold
Institute for Mathematics and its Applications
University of Minnesota
Minneapolis, MN 55455
USA
http://www.ima.umn.edu/~arnold/

Pavel B. Bochev
Sandia National Laboratories
Computational Mathematics and Algorithms Department
Alburquerque, NM 87185-1110
USA
http://math.uta.edu/~bochev/

Richard B. Lehoucq
Sandia National Laboratories
Computational Mathematics and Algorithms Department
Alburquerque, NM 87185-1110
USA
http://www.cs.sandia.gov/~rlehoucq

Roy A. Nicolaides
Department of Mathematical Sciences
Carnegie Mellon University
Pittsburgh, PA 15213-3890
USA
http://www.math.cmu.edu/people/fac/nicolaides.html

Mikhail Shashkov
Theoretical Division
Los Alamos National Laboratory
Los Alamos, NM 87545
USA
http://cnls.lanl.gov/~shashkov

Series Editors
Douglas N. Arnold
Arnd Scheel
Institute for Mathematics and its Applications
University of Minnesota
Minneapolis, MN 55455
USA

Mathematics Subject Classification (2000): 65N06, 65N12, 65N30, 65N35, 65D25, 65D30, 58A10, 58A12, 14F40, 58A15, 58A14, 55U10, 55U15, 53A45

Library of Congress Control Number: 2006921649

ISBN-10: 0-387-30916-0 Printed on acid-free paper.
ISBN-13: 978-0387-30916-3

Printed in the United States of America. (MVY)

Camera-ready copy provided by the IMA.

9 8 7 6 5 4 3 2 1

springer.com

FOREWORD

This IMA Volume in Mathematics and its Applications

COMPATIBLE SPATIAL DISCRETIZATIONS

contains papers presented at a highly successful IMA Hot Topics Workshop: Compatible Spatial Discretizations for Partial Differential Equations. The event which was held on May 11-15, 2004 was organized by Douglas N. Arnold (IMA, University of Minnesota), Pavel B. Bochev (Computational Mathematics and Algorithms Department, Sandia National Laboratories), Richard B. Lehoucq (Computational Mathematics and Algorithms Department, Sandia National Laboratories), Roy A. Nicolaides (Department of Mathematical Sciences, Carnegie-Mellon University), and Mikhail Shashkov (MS-B284, Group T-7, Theoretical Division, Los Alamos National Laboratory). We are grateful to all participants and organizers for making this a very productive and stimulating meeting, and we would like to thank the organizers for their role in editing this proceeding.

We take this opportunity to thank the National Science Foundation for its support of the IMA and the Department of Energy for providing additional funds to support this workshop.

Series Editors

Douglas N. Arnold, Director of the IMA

Arnd Scheel, Deputy Director of the IMA

PREFACE

In May 2004 over 80 mathematicians and engineers gathered in Minneapolis for a "hot topics" IMA workshop to talk, argue and conjecture about compatibility of spatial discretizations for Partial Differential Equations. We define *compatible*, or *mimetic*, spatial discretizations as those that inherit or mimic fundamental properties of the PDE such as topology, conservation, symmetries, and positivity structures and maximum principles.

The timing and place for this workshop were not incidental. PDEs are one of the principal modeling tools in science and engineering and their numerical solution is the workhorse of computational science. However, historically, numerical methods for PDEs such as finite differences (FD), finite volumes (FV) and finite elements (FE) evolved separately and until recently, in relative isolation from each other. This situation started to change about two decades ago when researchers working in these areas began to realize that robust and accurate discrete models share more than just a passing resemblance to each other. While FD, FV and FE methods have all developed specific approaches to compatibility, their successful discrete models were found to operate in what essentially came down to a discrete vector calculus structure replete with algebraic versions of the vector calculus identities and theorems.

Because of their more explicit reliance on grid topology, FD and FV methods recognized the role of geometry earlier than FE methods. For FEM compatibility criteria evolved from variational theories and assumed the form of powerful, but non-constructive inf-sup conditions. This changed in the 80s with the pioneering work of Bossavit who brought to light fundamental connections between the DeRham complex and compatible FEs for the Maxwell's equations. Consequently, research in applications of differential geometry, exterior calculus and algebraic topology to numerical PDEs intensified. This research led to important advances in understanding of spatial compatibility and connections between different compatible discrete models. Among the payoffs from this work were development of new stable FE models for linear elasticity and rigorous convergence analysis of mimetic FD by variational tools.

Thus, the organizers felt that the time was ripe for the researchers working in this field to get together and compare notes. The relevance of the topic and its impact on computational sciences helped to attract attendees from a broad cross-section of the community. The stature of IMA, its tradition and experience in organizing small focused workshops and its dedicated staff made the Institute a natural venue for this gathering.

This volume, co-edited by the workshop organizers, is representative of the topics discussed during the meeting. The papers, based on a subset of the plenary talks, offer the reader a snapshot of the current trends and developments in compatible and mimetic spatial discretizations. Abstracts and presentation slides from the workshop can be accessed at `http://www.ima.umn.edu/talks/workshops/5-11-15.2004/`.

While many of the contributions in this volume address questions regarding spatial compatibility, each paper offers a unique perspective and insight into specific techniques and approaches. Arnold *et al* focus on a *homological approach* to stability of mixed FE which, in the recent years, has greatly contributed to the understanding of mixed methods and the development of stable methods for previously intractable problems. The first part of their contribution deals with two polynomial versions of the DeRham complex. One complex involves homogeneous polynomial spaces of decreasing degree and the second is obtained with the help of the Kozsul differential. The two polynomial complexes contain generalizations of well-known finite element pairs such as Raviart-Thomas, BDM and Nedelec elements of first and second kinds. Then, they proceed to show how to use polynomial sub-complexes and commuting diagrams to obtain stability of mixed methods. The second part of Arnold *et al* deals with application of the homological approach to *mixed linear elasticity.* They show that a differential complex relevant to mixed linear elasticity can be obtained from the DeRham complex. An analogous construction is used to develop a discrete elasticity complex from a polynomial DeRham complex and results in new stable finite element spaces for mixed linear elasticity.

The paper by Boffi examines compatibility issues that arise in mixed finite element approximations to *eigenvalue problems.* A surprising counterexample shows that the classical Brezzi theory, which provides sufficient compatibility conditions for mixed methods, is not enough to guarantee the absence of spurious modes in mixed approximations of eigenvalue problems. After theoretical explanation and practical demonstration of this behavior, Boffi proceeds to develop sufficient and necessary conditions for correct mixed eigenmode discretizations and then gives several examples for possible application of the eigenvalue compatibility theory. Among other things, Boffi shows that good approximation of evolution problems in mixed form is contingent upon spectral convergence of the related eigenvalue problem, that is, it is also a subject to compatibility conditions beyond that of the classical Brezzi theory.

Application of algebraic topology to compatible discretizations is the central topic of Bochev and Hyman. They use two basic mappings between differential forms and cochains to define a framework that supports mutually consistent operations of differentiation and integration. This is accomplished by a set of *natural* operations that induce a set of *derived* discrete operations. The resulting framework has a combinatorial Stokes theorem and preserves the invariants of the De Rham cohomology groups.

The key concept of their approach is the natural inner product on cochains. This inner product is sufficient to generate a combinatorial Hodge theory on cochains but avoids complications attendant in the construction of efficient discrete Hodge-star operators. The framework provides an abstraction that includes examples of mixed FE, mimetic FD and FV methods. The paper also describes how these methods result from a choice of a reconstruction operator and explains when they are equivalent.

An interesting perspective on compatibility and how it affects *Discontinuous Galerkin* (DG) methods is presented in the paper by Barth. Because of a number of valuable computational properties, DG methods are attracting significant attention. Their origins for elliptic problems can be traced to interior penalty methods and so they are not compatible in the sense of mixed finite element methods. Using the Maxwell's equations and ideal MHD, Barth draws attention to the different roles played by their *involutions* for the formulation of energy-stable DG methods. The Maxwell's equations are naturally expressed in symmetric form, while symmetrization of MHD utilizes the involution as a necessary ingredient. This leads to fundamental differences in energy stability of the associated DG methods. Barth shows that imposing continuity of the magnetic flux at interelement boundaries is beneficial for energy stability of DG for MHD, while, somewhat counterintuitively, this condition is not required for DG discretizations of the Maxwells equations.

A *co-volume* approach to compatible discretizations is discussed by Trapp and Nicolaides. Building upon a solid body of work in classical FV methods, they use Voronoi-Delaunay grids to discretize differential forms. Their approach exploits the Voronoi-Delaunay grid complex to obtain a primal and a dual set of discrete forms connected by a local discrete Hodge operator. This leads to algebraic PDE models with particularly simple and attractive structure and a discrete setting where both the primal and the dual discrete differential operators have *local* stencils. In addition, the primal and dual operators are adjoint with respect to a co-volume inner product, which immediately gives rise to a discrete Hodge decomposition. To illustrate the co-volume approach, Trapp and Nicolaides develop compatible discretizations for two instances of the Hodge Laplacian in three-dimensions.

The two contributions by Wheeler and Yotov, and by Aavatsmark *et al* examine compatible methods for problems arising in *reservoir simulation* and *porous media* flows. The task of devising compatible methods for these applications is greatly complicated by the need to reconcile mathematical compatibility conditions with grid structure imposed by *geological features* such as layering, faults and crossbeddings. As a result, methods for geophysical applications have traditionally favored quadrilateral and hexahedral grids, which can cause some problems in the reconstruction of vector fields from normal components. In addition, permeability tensor in reservoir models often has strong anisotropy and/or discontinuities

along geological features. The two papers offer two alternative approaches that lead to cell-centered, locally conservative schemes. Aavatsmark *et al* adopt a Finite Volume approach based on the concept of multipoint flux approximation (MPFA). In this approach, fluxes are defined by using linear reconstruction of the potential subject to specific flux and potential continuity conditions. In contrast, Wheeler and Yotov start from a mixed variational formulation and then design a quadrature rule that allows for a local elimination of the velocities and results in a symmetric and positive definite cell-centered potential matrix. The result is a method that is related to MPFA and has a variational formulation. This allows them to leverage approximation theory from mixed methods and prove second order convergence of the scalar at the cell-centers.

A hallmark of many compatible discretizations, such as Raviart-Thomas elements, Nedelec elements or mimetic Finite Differences, is the use of normal or tangential vector components. This enables discrete versions of the divergence and the Stokes theorems but poses problems when vector fields are needed to compute *vector derived quantities* such as kinetic energy or advective terms. The reconstructed fields may fail to provide local conservation of the kinetic energy and the momentum. Reconstruction of vector fields from dispersed data is the subject of the contribution by Perot *et al.* Their paper discusses relationship between three low order reconstruction operators. Two of these operators are related to mimetic finite difference and finite element methods, respectively. The third one is a new reconstruction approach proposed by the authors. Perot *et al* discuss how explicit reconstruction can be used to define discrete Hodge star operators. The paper then focuses on reconstruction approaches that can provide *local conservation* for vector derived quantities such as momentum and kinetic energy.

Software frameworks and computational experiments for compatible methods are communicated in the papers by Demkowicz and Kurtz, and by White *et al.* Both papers consider compatible methods for the Maxwell's equations. White *et al* describe an extensible, object-oriented C++ framework that closely mimics the structure of differential form calculus. The emphasis is on *high-order* finite element basis functions that form a discrete De Rham complex and have the relevant commuting diagram properties. As a result, any electromagnetics problem that can be cast in the language of differential forms can be easily modeled by their framework. The flexibility of the framework is illustrated by solving resonant cavity, wave propagation and eddy current problems. Demkowicz and Kurtz develop an *hp*-adaptive implementation of a coupled finite element/infinite element approximation for *exterior wave propagation* problems. The novel aspect of the paper is a family of infinite elements that satisfies an exact sequence property. The elements in the new sequence are obtained by multiplying basis functions from a standard polynomial De Rham complex by an exponential factor that comes from the far-field pattern. The exactness is with

respect to similarly modified differential operators. A series of experiments confirms stability of the coupling and exponential rate of convergence obtained by automatic *hp*-adaptivity.

In closing, the editors want to thank the authors for contributing to this volume and their cooperation in the editorial process. Special thanks are also due to Patricia V. Brick and Dzung N. Nguyen for the excellent coordination of the production schedule and assistance in the final preparation of the papers for the publisher. Dr. C. Romine, formerly of the DOE'S MICS Applied Mathematics Research program, offered enthusiastic support and encouragement during the preparation of the workshop. His help is greatly appreciated. Funding for the workshop was provided by the DOE Office of Science's Advanced Scientific Computing Research (ASCR) Applied Mathematics Research Program.

Douglas N. Arnold
Institute for Mathematics and its Applications
University of Minnesota

Pavel B. Bochev
Computational Mathematics and Algorithms Department
Sandia National Laboratories

Richard B. Lehoucq
Computational Mathematics and Algorithms Department
Sandia National Laboratories

Roy A. Nicolaides
Department of Mathematical Sciences
Carnegie Mellon University

Mikhail Shashkov
Theoretical Division
Los Alamos National Laboratory

CONTENTS

NUMERICAL CONVERGENCE OF THE MPFA O-METHOD FOR GENERAL QUADRILATERAL GRIDS IN TWO AND THREE DIMENSIONS

IVAR AAVATSMARK*, GEIR TERJE EIGESTAD†, AND RUNHILD AAE KLAUSEN‡

Abstract. This paper presents the MPFA O-method for quadrilateral grids, and gives convergence rates for the potential and the normal velocities. The convergence rates are estimated from numerical experiments. If the potential is in $H^{1+\alpha}$, $\alpha > 0$, the found L^2 convergence order on rough grids in physical space is $\min\{2, 2\alpha\}$ for the potential and $\min\{1, \alpha\}$ for the normal velocities. For smooth grids the convergence order for the normal velocities increases to $\min\{2, \alpha\}$. The O-method is exact for uniform flow on rough grids. This also holds in three dimensions, where the cells may have nonplanar surfaces.

Key words. Control-volume discretization, anisotropy, inhomogeneity, convergence.

AMS(MOS) subject classifications. 65M06, 76S05, 35R05.

1. Introduction.

We consider a control-volume discretization of the model equation

$$\operatorname{div} \boldsymbol{q} = Q, \qquad \boldsymbol{q} = -\boldsymbol{K} \operatorname{grad} u \tag{1.1}$$

on a quadrilateral grid. The conductivity $\boldsymbol{K}$ is required to be symmetric and positive definite.

Our applications are solutions of multiphase flow equations in reservoir simulation. These equations contain an elliptic operator similar to the left-hand side of (1.1), and this motivates our study. The multiphase flow equations in reservoir simulation have properties which constrain the choice of grid and discretization technique used for the elliptic operator. By reformulation of the flow equations, a coupled set of parabolic equations appear. However, one of these equations (the pressure equation) has an elliptic character, while the other equations (the saturation equations) have hyperbolic character with a strongly nonlinear convective term. Phase transitions which are strongly pressure dependent, may occur.

Due to the hyperbolicity and the strong nonlinearity of the saturation equations, we require that the discretization scheme should be locally conservative. Also, since the phase transitions are pressure dependent, we require that the pressure is evaluated at the same point as the saturations.

*Center for Integrated Petroleum Research, University of Bergen, NO-5020 Bergen, Norway (ivar.aavatsmark@cipr.uib.no).

†(geirte@mi.uib.no).

‡(runhildk@ifi.uio.no).

This motivates the use of a control-volume scheme for (1.1), with evaluation of the dependent variable u at the center of the cells.

Stability for nonlinear hyperbolic equations is normally achieved by requiring that the chosen scheme is monotone. In reservoir simulation, stability is accomplished by upstream weighting of the phase flow. In a fully implicit scheme for the flow equations, a simple upstream weighting can only be done if the method for the elliptic operator in (1.1) yields the flux at the edges as an explicit function of the potential u at some neighboring cell centers.

The grids used in reservoir simulation are normally quadrilateral grids with an aspect ratio which strongly deviates from unity. To avoid the difficulties of upscaling, the grid layering is normally determined by the geological layering. This often yields almost rectangular grids with homogeneous cell properties. At faults or in near-well regions, grids with a more complex geometry may be preferred.

In reservoir simulation the conductivity $\boldsymbol{K}$ of (1.1) is given by the absolute permeability. It is a tensor which often has a strong anisotropy. Because of the symmetry of the tensor, the principal directions are orthogonal. The principal directions are often aligned with, and normal to, the grid layering. For layers with varying thickness, this is only approximately fulfilled. If the layers contain crossbeddings, the principal directions of the tensor may be arbitrary.

The absolute permeability may vary strongly in reservoir simulation. Since the potential node should be located at the cell centers, it is therefore important that the discrete resistance between two nodes honors the strong heterogeneity. This means that for one-dimensional flow, the method should give a conductance equal to a harmonic average of the cell conductances.

In summary, we will describe a control-volume method for equation (1.1) which yields the flux at the edges as an explicit function of the potential at the cell centers. The conductivity should be symmetric and positive definite, but its principal directions may be arbitrary compared to the grid directions. The discrete resistance between cell nodes must honor the heterogeneity. We will confine ourselves to quadrilateral grids.

One method with the above properties is the MPFA (Multipoint Flux Approximation) method. It can be applied to quadrilateral grids [1, 2, 4, 8, 18] and to unstructured grids [3, 5, 6, 7, 17], see [1] for a more complete bibliography.

In this paper we introduce the method in a new way which emphasizes the connection between anisotropy and grid skewness. Then we present convergence results for the method. These supplement the results of [9].

There are many variants of the MPFA method; in this paper we only discuss the method known as the *O-method.*

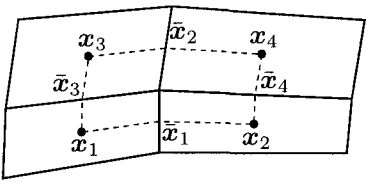

FIG. 1. *Interaction volume (bounded by the dashed lines).*

2. The MPFA O-method. In this section we derive the equations for the MPFA O-method in two dimensions. Consider the four quadrilateral cells with a common vertex in Fig. 1. The cells have cell centers $\boldsymbol{x}_k$, and the edges have midpoints $\bar{\boldsymbol{x}}_i$. The points are enumerated locally as shown in the figure. Between the cell centers and the midpoints of the edges we draw lines (shown as dashed lines in the figure). These lines bound an area around each vertex which is called an *interaction volume* (also referred to as an interaction region in previous papers). Hence, the interaction volume in the figure is the polygon with corners $\boldsymbol{x}_1\bar{\boldsymbol{x}}_1\boldsymbol{x}_2\bar{\boldsymbol{x}}_4\boldsymbol{x}_4\bar{\boldsymbol{x}}_2\boldsymbol{x}_3\bar{\boldsymbol{x}}_3$.

Within the interaction volume there are four half edges. Below, we will show how to determine the flux through these half edges from the interaction between the four cells. When the fluxes through the four half edges in an interaction volume around a vertex are determined, we may repeat the procedure for the interaction volumes of the other vertices. In this way, the flux through all the half edges in a grid will be determined. When the fluxes through the two half edges of an entire edge are known, we may add them to get an expression for the flux through the entire edge. An assembly procedure may then be performed to construct a system of difference equations corresponding to Eq. (1.1).

This procedure also holds for the half edges at the boundary of a domain, if the boundary conditions are given as homogeneous Neumann conditions. Outside the real cells we can put a strip of artificial cells with vanishing conductivity. The same procedure as described above for the interaction volumes around the vertices at the boundary then gives the flux through the half edges separating the real boundary cells. More general boundary conditions are discussed in [9].

We now show how the fluxes through the four half edges in an interaction volume may be determined. In each of the four cells of the interaction volume, the potential u is expressed as a linear function. The value of the potential in each cell center determines one of the coefficients in each cell for these linear functions. The linear function determines the flux through the half edges of the cell and the potential at the half edges. We require that the fluxes through the half edges in an interaction volume are continuous, and that the potentials at the midpoints of the edges are continuous. This yields eight equations for the determination of the unknown coefficients of the linear functions in the cells.

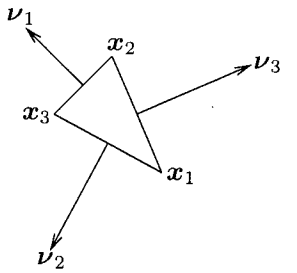

FIG. 2. *Triangle with edge normals* ν_i.

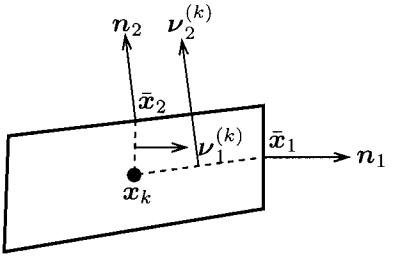

FIG. 3. *Normal vectors in cell k.*

Every linear function is decribed by three coefficients, but one of them is already determined throught the potential value at the cell center. All together there are therefore eight unknown coefficients for the linear functions. They are determined through the eight continuity equations. Note that the continuity principles used here, are exactly the same as the principles used to derive the classical two-point flux formula [1].

Every cell is shared among four interaction volumes. The linear functions for the potential in a cell, may vary from interaction volume to interaction volume. This does not cause any difficulties, since the linear functions are only used to determine an expression for the flux. In the resulting difference equations, only the potential at the cell centers appears.

For each interaction volume, the linear functions in each cell may be determined in the following way. On a triangle with corners $\boldsymbol{x}_i$, $i = 1, 2, 3$, any linear function may be described by

$$u(\boldsymbol{x}) = \sum_{i=1}^{3} u_i \phi_i(\boldsymbol{x}). \tag{2.1}$$

Here, u_i is the value of $u(\boldsymbol{x})$ at vertex i, and $\phi_i(\boldsymbol{x})$ is the linear basis function defined by $\phi_i(\boldsymbol{x}_j) = \delta_{i,j}$. The gradient is easily calculated to be

$$\operatorname{grad} \phi_i = -\frac{1}{2F} \boldsymbol{\nu}_i, \tag{2.2}$$

where F is the area of the triangle. Here, $\boldsymbol{\nu}_i$ is the outer normal vector of the edge lying opposite to vertex i, see Fig. 2. The length of $\boldsymbol{\nu}_i$ equals the length of the edge to which it is normal. For these normal vectors the following relation holds

$$\sum_{i=1}^{3} \boldsymbol{\nu}_i = \mathbf{0}. \tag{2.3}$$

Thus, the gradient expression of the potential in the triangle may be written

$$\operatorname{grad} u = -\frac{1}{2F} \sum_{i=1}^{3} u_i \boldsymbol{\nu}_i = -\frac{1}{2F} \left[(u_2 - u_1)\boldsymbol{\nu}_2 + (u_3 - u_1)\boldsymbol{\nu}_3 \right]. \tag{2.4}$$

Now consider the grid cell in Fig. 3. The grid cell has index k and cell center $\boldsymbol{x}_k$. Using local indices, the midpoints on the edges are denoted $\bar{\boldsymbol{x}}_1$ and $\bar{\boldsymbol{x}}_2$, and the associated normals on the connection lines between the cell center and the midpoints of the edges are denoted $\boldsymbol{\nu}_2^{(k)}$ and $\boldsymbol{\nu}_1^{(k)}$, see Fig. 3. Later, it will appear suitable to let the vectors $\boldsymbol{\nu}_i^{(k)}$ point in the direction of increasing global cell indices. In this cell we therefore reverse the direction of these vectors. Other locations of the points $\bar{\boldsymbol{x}}_1$ and $\bar{\boldsymbol{x}}_2$ on the edges are also allowed [8], but that will not be considered in this paper. Using the formula (2.4) on the triangle $\boldsymbol{x}_k\bar{\boldsymbol{x}}_1\bar{\boldsymbol{x}}_2$ yields

$$\operatorname{grad} u = \frac{1}{2F_k}\left[\boldsymbol{\nu}_1^{(k)}(\bar{u}_1 - u_k) + \boldsymbol{\nu}_2^{(k)}(\bar{u}_2 - u_k)\right], \tag{2.5}$$

where $\bar{u}_i = u(\bar{\boldsymbol{x}}_i)$, $i = 1, 2$, and $u_k = u(\boldsymbol{x}_k)$. Obviously, for Eq. (2.5) to be valid, the vectors $\boldsymbol{\nu}_1^{(k)}$ and $\boldsymbol{\nu}_2^{(k)}$ have to be linearly independent. Each of the edges can be associated with a global direction, defined through the unit normal $\boldsymbol{n}_i$. We will also let $\boldsymbol{n}_i$ point in the direction of increasing global cell indices. The flux through half edge i as seen form cell k is denoted $f_i^{(k)}$. The flux may now be determined from the gradient of the potential in the cell. For the fluxes in the cell in Fig. 3, the following expression appears

$$\begin{aligned}\begin{bmatrix} f_1^{(k)} \\ f_2^{(k)} \end{bmatrix} &= -\begin{bmatrix} \Gamma_1\boldsymbol{n}_1^{\mathrm{T}} \\ \Gamma_2\boldsymbol{n}_2^{\mathrm{T}} \end{bmatrix} \boldsymbol{K}_k \operatorname{grad} u \\ &= -\frac{1}{2F_k}\begin{bmatrix} \Gamma_1\boldsymbol{n}_1^{\mathrm{T}} \\ \Gamma_2\boldsymbol{n}_2^{\mathrm{T}} \end{bmatrix} \boldsymbol{K}_k \begin{bmatrix} \boldsymbol{\nu}_1^{(k)} & \boldsymbol{\nu}_2^{(k)} \end{bmatrix} \begin{bmatrix} \bar{u}_1 - u_k \\ \bar{u}_2 - u_k \end{bmatrix},\end{aligned} \tag{2.6}$$

where Γ_i is the length of half edge i. By defining the matrix

$$\begin{aligned}\boldsymbol{G}_k &= \frac{1}{2F_k}\begin{bmatrix} \Gamma_1\boldsymbol{n}_1^{\mathrm{T}} \\ \Gamma_2\boldsymbol{n}_2^{\mathrm{T}} \end{bmatrix} \boldsymbol{K}_k \begin{bmatrix} \boldsymbol{\nu}_1^{(k)} & \boldsymbol{\nu}_2^{(k)} \end{bmatrix} \\ &= \frac{1}{2F_k}\begin{bmatrix} \Gamma_1\boldsymbol{n}_1^{\mathrm{T}}\boldsymbol{K}_k\boldsymbol{\nu}_1^{(k)} & \Gamma_1\boldsymbol{n}_1^{\mathrm{T}}\boldsymbol{K}_k\boldsymbol{\nu}_2^{(k)} \\ \Gamma_2\boldsymbol{n}_2^{\mathrm{T}}\boldsymbol{K}_k\boldsymbol{\nu}_1^{(k)} & \Gamma_2\boldsymbol{n}_2^{\mathrm{T}}\boldsymbol{K}_k\boldsymbol{\nu}_2^{(k)} \end{bmatrix},\end{aligned} \tag{2.7}$$

Eq. (2.6) may be written in the form

$$\begin{bmatrix} f_1^{(k)} \\ f_2^{(k)} \end{bmatrix} = -\boldsymbol{G}_k \begin{bmatrix} \bar{u}_1 - u_k \\ \bar{u}_2 - u_k \end{bmatrix}. \tag{2.8}$$

Now consider the interaction volume in Fig. 4. Through the normal vectors introduced here, the matrix $\boldsymbol{G}_k$ is defined for all the four cells. Thus,

$$\begin{bmatrix} f_1^{(1)} \\ f_3^{(1)} \end{bmatrix} = -\boldsymbol{G}_1 \begin{bmatrix} \bar{u}_1 - u_1 \\ \bar{u}_3 - u_1 \end{bmatrix}, \qquad \begin{bmatrix} f_1^{(2)} \\ f_4^{(2)} \end{bmatrix} = -\boldsymbol{G}_2 \begin{bmatrix} u_2 - \bar{u}_1 \\ \bar{u}_4 - u_2 \end{bmatrix}, \tag{2.9}$$

$$\begin{bmatrix} f_2^{(3)} \\ f_3^{(3)} \end{bmatrix} = -\boldsymbol{G}_3 \begin{bmatrix} \bar{u}_2 - u_3 \\ u_3 - \bar{u}_3 \end{bmatrix}, \qquad \begin{bmatrix} f_2^{(4)} \\ f_4^{(4)} \end{bmatrix} = -\boldsymbol{G}_4 \begin{bmatrix} u_4 - \bar{u}_2 \\ u_4 - \bar{u}_4 \end{bmatrix}. \tag{2.10}$$

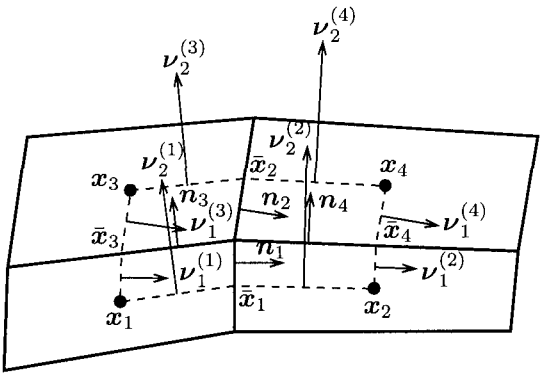

FIG. 4. *Normal vectors with local numbering in an interaction volume.*

Here, as before, $u_k = u(\boldsymbol{x}_k)$ and $\bar{u}_i = u(\bar{\boldsymbol{x}}_i)$, see Fig. 4. Compared to cell 1, we have reversed the directions of $\boldsymbol{\nu}_1^{(2)}$, $\boldsymbol{\nu}_2^{(3)}$, $\boldsymbol{\nu}_1^{(4)}$, and $\boldsymbol{\nu}_2^{(4)}$ (see Fig. 4). The differences $\bar{u}_1 - u_2$, $\bar{u}_3 - u_3$, $\bar{u}_2 - u_4$, and $\bar{u}_4 - u_4$ therefore appear in the expressions (2.9) and (2.10) with opposite sign.

The continuity conditions for the fluxes now yield

$$\begin{aligned} f_1 &= f_1^{(1)} = f_1^{(2)}, \\ f_2 &= f_2^{(4)} = f_2^{(3)}, \\ f_3 &= f_3^{(3)} = f_3^{(1)}, \\ f_4 &= f_4^{(2)} = f_4^{(4)}. \end{aligned} \tag{2.11}$$

Using the expressions (2.9) and (2.10), these equations become

$$\begin{aligned} f_1 &= -g_{1,1}^{(1)}(\bar{u}_1 - u_1) - g_{1,2}^{(1)}(\bar{u}_3 - u_1) = g_{1,1}^{(2)}(\bar{u}_1 - u_2) - g_{1,2}^{(2)}(\bar{u}_4 - u_2), \\ f_2 &= g_{1,1}^{(4)}(\bar{u}_2 - u_4) + g_{1,2}^{(4)}(\bar{u}_4 - u_4) = -g_{1,1}^{(3)}(\bar{u}_2 - u_3) + g_{1,2}^{(3)}(\bar{u}_3 - u_3), \\ f_3 &= -g_{2,1}^{(3)}(\bar{u}_2 - u_3) + g_{2,2}^{(3)}(\bar{u}_3 - u_3) = -g_{2,1}^{(1)}(\bar{u}_1 - u_1) - g_{2,2}^{(1)}(\bar{u}_3 - u_1), \\ f_4 &= g_{2,1}^{(2)}(\bar{u}_1 - u_2) - g_{2,2}^{(2)}(\bar{u}_4 - u_2) = g_{2,1}^{(4)}(\bar{u}_2 - u_4) + g_{2,2}^{(4)}(\bar{u}_4 - u_4). \end{aligned} \tag{2.12}$$

The Eqs. (2.12) contain the edge values $\bar{u}_1$, $\bar{u}_2$, $\bar{u}_3$, and $\bar{u}_4$. Tacitly we have here used the same expression for the edge value of the cells at each side of an edge, and thereby implicitly demanded continuity of the potential at the points $\bar{\boldsymbol{x}}_1$, $\bar{\boldsymbol{x}}_2$, $\bar{\boldsymbol{x}}_3$, and $\bar{\boldsymbol{x}}_4$.

If the matrix $\boldsymbol{G}_k$ is diagonal for all cell indices k, the grid is called $\boldsymbol{K}$-*orthogonal*. The system of equations (2.12) is then no longer coupled, and the flux through the edges can be determined by eliminating the edge values $\bar{u}_i$. This gives a two-point flux expression. If the grid is not $\boldsymbol{K}$-orthogonal, the edge values $\bar{u}_i$ may still be eliminated in each interaction volume. We then proceed in the following way.

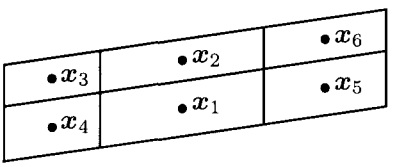

FIG. 5. *Flux stencil.*

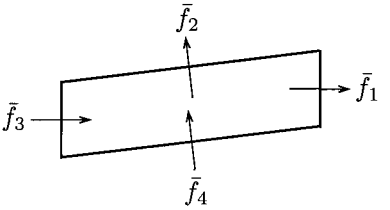

FIG. 6. *Flux through the cell edge of a cell.*

The fluxes of the system of equations (2.12) can be collected in the vector $\boldsymbol{f}$ defined by $\boldsymbol{f} = [f_1, f_2, f_3, f_4]^{\mathrm{T}}$. The system of equations further contains the potential values of the cell centers $\boldsymbol{u} = [u_1, u_2, u_3, u_4]^{\mathrm{T}}$ and the potential values at the midpoints of the cell edges $\boldsymbol{v} = [\bar{u}_1, \bar{u}_2, \bar{u}_3, \bar{u}_4]^{\mathrm{T}}$. The expressions on each side of the left equality sign of (2.12) can therefore be written on the form

$$\boldsymbol{f} = \boldsymbol{C}\boldsymbol{v} + \boldsymbol{F}\boldsymbol{u}. \tag{2.13}$$

The expressions on each side of the right equality sign in the system of equations (2.12) may after a reorganization be written in the form

$$\boldsymbol{A}\boldsymbol{v} = \boldsymbol{B}\boldsymbol{u}. \tag{2.14}$$

Hence, $\boldsymbol{v}$ may be eliminated by solving Eq. (2.14) with respect to $\boldsymbol{v}$ and putting $\boldsymbol{v} = \boldsymbol{A}^{-1}\boldsymbol{B}\boldsymbol{u}$ into (2.13). This gives the flux expression

$$\boldsymbol{f} = \boldsymbol{T}\boldsymbol{u}, \tag{2.15}$$

where

$$\boldsymbol{T} = \boldsymbol{C}\boldsymbol{A}^{-1}\boldsymbol{B} + \boldsymbol{F}. \tag{2.16}$$

The entries of the matrix $\boldsymbol{T}$ are called *transmissibility coefficients.* Equation (2.15) gives the flux through the half edges expressed by the potential values at the cell centers of an interaction volume.

Having determined the flux expression for all half edges, the two flux expressions of the two half edges which constitute an edge, can be added. This is shown in Fig. 5, where the cells 1, 2, 3, and 4 constitute one interaction volume, and the cells 1, 2, 5, and 6 constitute another. The flux stencil of the edge between cell 1 and 2 will therefore consist of the six cells of the figure. When the flux expressions have been found, these may be used in a discrete variant of Eq. (1.1). For the cell shown in Fig. 6 this yields the equation

$$\bar{f}_1 + \bar{f}_2 - \bar{f}_3 - \bar{f}_4 = VQ, \tag{2.17}$$

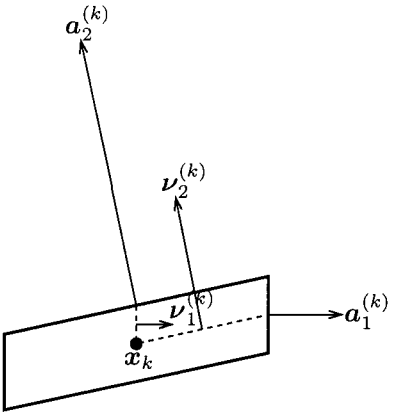

FIG. 7. *Normal vectors in parallelogram cells.*

where $\bar{f}_i$ is the flux through the entire edge i, V is the volume of the cell, and the source term Q has been approximated by a constant in the cell. This is a difference equation with u at the cell centers as the unknowns.

If two neighboring cells have vanishing conductivity, the corresponding row in the matrix $\boldsymbol{A}$ vanishes, and hence, the matrix $\boldsymbol{A}$ is singular. Because there is no need to determine the flux across the interfaces of cells with vanishing conductivity, the system may be reduced, and this will remove the singularity. However, it is more favorable to retain the system of unknowns and redefine the matrix $\boldsymbol{A}$ such that it becomes nonsingular. This is easiliy done by setting the diagonal elements of the vanishing rows in the matrix $\boldsymbol{A}$ equal to 1. The new system of equations has for the interfaces between cells with nonvanishing conductivity the same transmissibility coefficients as the reduced system.

For homogeneous media, test runs indicate that the matrix $\boldsymbol{A}$ is well conditioned, also for geometrically distorted cells. On the tested rough grids, the condition number satisfied $\text{cond}_2 \boldsymbol{A} < 50$.

If cell k in Fig. 3 is a parallelogram, the expression for the matrix $\boldsymbol{G}_k$, Eq. (2.7), is simplified. For a parallelogram-shaped cell with index k, we denote the normal vectors of the edges with $\boldsymbol{a}_i^{(k)}$, $i = 1, 2$. These have length equal to the length of the edges. The normal vectors are shown in Fig. 7. Obviuosly, $\Gamma_i \boldsymbol{n}_i = \boldsymbol{a}_i^{(k)}/2$ and $\boldsymbol{\nu}_i^{(k)} = \boldsymbol{a}_i^{(k)}/2$. Further, $F_k = V_k/8$, where V_k is the area of cell k. It follows that for a parallelogram-shaped cell,

$$\boldsymbol{G}_k = \frac{1}{V_k} \begin{bmatrix} \boldsymbol{a}_1^{(k)} & \boldsymbol{a}_2^{(k)} \end{bmatrix}^{\mathrm{T}} \boldsymbol{K}_k \begin{bmatrix} \boldsymbol{a}_1^{(k)} & \boldsymbol{a}_2^{(k)} \end{bmatrix}. \tag{2.18}$$

Letting $\boldsymbol{J}_k = \begin{bmatrix} \boldsymbol{a}_1^{(k)}, & \boldsymbol{a}_2^{(k)} \end{bmatrix}$, one gets $V_k = |\det \boldsymbol{J}_k|$, and Eq. (2.18) becomes

$$\boldsymbol{G}_k = \frac{1}{|\det \boldsymbol{J}_k|} \boldsymbol{J}_k^{\mathrm{T}} \boldsymbol{K}_k \boldsymbol{J}_k. \tag{2.19}$$

Hence, for a parallelogram cell the tensor $\boldsymbol{G}_k$ is symmetric. Equation (2.19) is a congruence transformation. Thus, the tensor $\boldsymbol{G}_k$, as given by (2.18), is symmetric and positive definite if and only if $\boldsymbol{K}_k$ has these properties. If the tensor $\boldsymbol{G}_k$ is diagonal for all cell indices k, i.e., if

$$\left(\boldsymbol{a}_i^{(k)}\right)^{\mathrm{T}} \boldsymbol{K}_k \boldsymbol{a}_j^{(k)} = 0, \qquad i \neq j, \tag{2.20}$$

then the grid is $\boldsymbol{K}$-orthogonal.

In the matrix $\boldsymbol{G}_k$ it is sometimes useful to perform a splitting, such that anisotropy and grid skewness appears in one matrix and the mesh distances in another. If $\Delta\eta_k$ is the length of $\boldsymbol{a}_1^{(k)}$ and $\Delta\xi_k$ is the length of $\boldsymbol{a}_2^{(k)}$, then for a parallelogram grid,

$$\boldsymbol{G}_k = \frac{1}{\Delta\xi_k \Delta\eta_k} \boldsymbol{D}_k \boldsymbol{H}_k \boldsymbol{D}_k, \tag{2.21}$$

where

$$\begin{aligned} \boldsymbol{H}_k &= \frac{1}{\det[\boldsymbol{n}_1,\ \boldsymbol{n}_2]} \begin{bmatrix} \boldsymbol{n}_1 & \boldsymbol{n}_2 \end{bmatrix}^{\mathrm{T}} \boldsymbol{K}_k \begin{bmatrix} \boldsymbol{n}_1 & \boldsymbol{n}_2 \end{bmatrix} \\ &= \frac{1}{\det[\boldsymbol{n}_1,\ \boldsymbol{n}_2]} \begin{bmatrix} \boldsymbol{n}_1^{\mathrm{T}} \boldsymbol{K}_k \boldsymbol{n}_1 & \boldsymbol{n}_1^{\mathrm{T}} \boldsymbol{K}_k \boldsymbol{n}_2 \\ \boldsymbol{n}_2^{\mathrm{T}} \boldsymbol{K}_k \boldsymbol{n}_1 & \boldsymbol{n}_2^{\mathrm{T}} \boldsymbol{K}_k \boldsymbol{n}_2 \end{bmatrix}, \end{aligned} \tag{2.22}$$

and

$$\boldsymbol{D}_k = \operatorname{diag}(\Delta\eta_k,\ \Delta\xi_k). \tag{2.23}$$

Here, $\boldsymbol{n}_i$ is the unit normal vector which is parallel with $\boldsymbol{a}_i^{(k)}$, see Fig. 7. If $\boldsymbol{H}_k$ is diagonal, the grid is $\boldsymbol{K}$-orthogonal.

2.1. Extension to three dimensions. The principles of the MPFA O-method carry over to three dimensions. In three dimensions, an interaction volume contains 8 subcells and 12 interfaces, see Fig. 8. The linear functions in the eight cells are described by 32 coefficients. Eight of these are determined by the potential values at the cell centers. The rest of them are determined by the two continuity conditions at each of the 12 interfaces: the flux is required to be continuous at the interfaces, and the potential is required to be continuous at the interface midpoints.

The generalization of the equations of section 2 to three dimensions is straight forward. However, a three-dimensional cell described by its eight corners, generally does not have planar surfaces. The unit normal vector $\boldsymbol{n}_i$ of an interface is therefore not a constant across the interface. This can be accounted for by integrating the normal vector over the interface of the subcell in question. If a cell interface has corners $\boldsymbol{x}_k$, $k = 1, \ldots, 4$, see Fig. 9, the integrated normal vector over the interface of the subcell at vertex $\boldsymbol{x}_1$ is

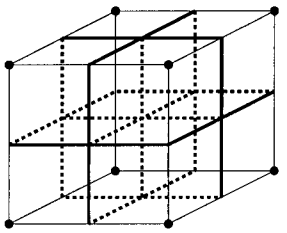

FIG. 8. *Tree-dimensional interaction volume (thin lines) with 8 subcells and 12 interfaces (thick lines).*

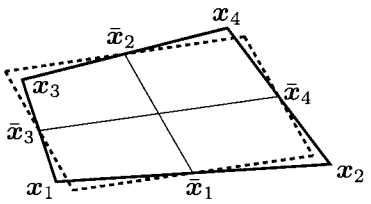

FIG. 9. *Replacing a quadrilateral (solid) by its associated parallelogram (dashed).*

$$\hat{n} = \frac{1}{64}\Big[9(x_2 - x_1) \times (x_3 - x_1) + 3(x_2 - x_1) \times (x_4 - x_2) + 3(x_4 - x_3) \times (x_3 - x_1) + (x_4 - x_3) \times (x_4 - x_2)\Big]. \tag{2.24}$$

The vector $\hat{n}$ has length equal to the area of the subcell interface, see [1] for details.

2.2. Symmetrization. The method described above yields a system of equations

$$Mu = b. \tag{2.25}$$

This is the discrete approximation of Eq. (1.1). Since the differential operator of Eq. (1.1) is self adjoint, one would like the matrix M of Eq. (2.25) to be symmetric. Further, the matrix M should be positive definite, to ensure that (2.25) approximates an elliptic equation.

Unfortunately, on a general quadrilateral grid the matrix M is not symmetric. However, if the matrices G_k, given in Eq. (2.7), are symmetric, one may show that the matrix of coefficients M is symmetric [4]. Therefore, if all the cells are parallelograms (parallelepipeds in 3D), then the matrix of coefficients M is symmetric. For general quadrilaterals, this can be accomplished by replacing each cell with its associated parallelogram cell. This is shown for two dimensions in Fig. 9. The associated parallelogram is constructed as follows. Let $\bar{x}_k$, $k = 1, \ldots, 4$, be the four midpoints of the edges of the quadrilateral, see Fig. 9. Draw the lines $\bar{x}_1\bar{x}_2$ and $\bar{x}_3\bar{x}_4$. Through each of the midpoints $\bar{x}_1$ and $\bar{x}_2$, lines parallel to $\bar{x}_3\bar{x}_4$ are drawn. Through each of the midpoints $\bar{x}_3$ and $\bar{x}_4$, lines parallel to $\bar{x}_1\bar{x}_2$ are drawn. The resulting quadrilateral (shown with dashed lines in Fig. 9) is the associated parallelogram.

Replacing each quadrilateral with its associated parallelogram yields a symmetric MPFA method. However, the order of convergence is generally lower, as shown in subsection 3.1. The described symmetric MPFA method is equivalent to the method which appears when each quadrilateral is transformed to a reference space with a bilinear mapping, and the flux

is calculated in the reference space, using the Jacobian matrix evaluated at the cell center [1]. For a parallelogram, the matrix $\boldsymbol{J}^{-\mathrm{T}}$ of Eq. (2.19) equals the Jacobian matrix $\boldsymbol{dx}/\boldsymbol{d\xi}$ of the bilinear mapping.

3. Convergence. In this section we test the convergence properties of the MPFA O-method on quadrilateral grids by numerical experiments. In the derivation of the method, we made use of the cell center, without defining the location of this center. We will first test which location is the best in terms of convergence. Further, we investigate different grids for the same reference solution (on homogeneous media). We also compare the solutions obtained by discretizing on the physical quadrilaterals and discretizing on the associated parallelograms. Finally, we discuss the convergence rates on physical quadrilaterals for solutions with different smoothness. Most of the test runs are in 2D, but at the end we supplement with 3D test runs.

In this section, the potential u is termed the pressure as in reservoir simulation. Except for the test runs of subsection 3.2, the convergence rates are measured by the following discrete L^2 norms for both the pressures and the edge normal velocities [9],

$$\|u_h - u\|_{L^2} = \left(\sum_i V_i (u_{h,i} - u_i)^2 \right)^{1/2}, \tag{3.1}$$

$$\|q_h - q\|_{L^2} = \left(\sum_j \tfrac{1}{4} (V_{j+} + V_{j-})(q_{h,j} - q_j)^2 \right)^{1/2}. \tag{3.2}$$

Here, $q = \boldsymbol{q} \cdot \boldsymbol{n}$ is the edge normal velocity. Subscript h refers to the discrete solution. Further, V_i is the volume (area) of cell i, and $V_{j\pm}$ are the volumes of the two cells separated by edge j. The total volume of the simulated domains is for all test cases equal to unity.

3.1. 2D results in L^2 norm. Figure 10 shows some of the grids used in the test runs. One grid is constructed such that the entire grid has to account for an internal 120° grid line (Fig. 10.a). Another grid is a uniform parallelogram grid with internal acute angles of 45° (not shown in the figure). A third grid is a zig-zag parallelogram grid (Fig. 10.c).

A randomization may be performed for the grids [10, 11, 15]. By displacing the corners of the grid in Fig. 10.a by a random h^β pertubation, a grid with an arbitrary roughness appears. Such a rough grid is shown in Fig. 10.b. Finally, the grid shown in Fig. 10.d will be applied for a test case found in [8].

The first test cases are performed with the solution

$$u(x, y) = \cosh(\pi x) \cos(\pi y) \tag{3.3}$$

of the problem (1.1) on an isotropic, homogeneous medium. The boundary conditions are given by Dirichlet conditions, and are implemeted by interpolation [8, 9].

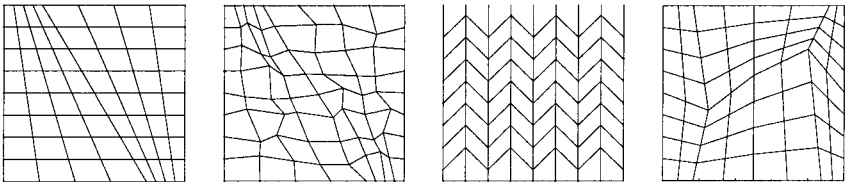

FIG. 10. *Grids used for simulations. From left ro right: (a): Smooth grid. (b): Random h^1 perturbution of the smooth grid. (c): Zig-zag parallelogram grid. (d): Grid used for simulation of* (3.7).

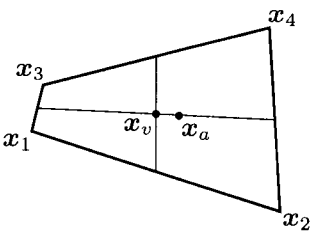

FIG. 11. *Vertex center x_v and area center x_a of a quadrilateral.*

We begin by testing different cell center locations. For quadrilaterals, there are two "natural" cell centers. The first is the vertex center

$$\boldsymbol{x}_v = \tfrac{1}{4}(\boldsymbol{x}_1 + \boldsymbol{x}_2 + \boldsymbol{x}_3 + \boldsymbol{x}_4), \tag{3.4}$$

where $\boldsymbol{x}_i$, $i = 1, \ldots, 4$, are the vertices of the quadrilateral. The second is the area center

$$\boldsymbol{x}_a = \frac{\int_V \boldsymbol{x}\, d\tau}{\int_V d\tau}, \tag{3.5}$$

where V is the quadrilateral. These centers are shown in Fig. 11. The area center is the barycenter of the area, whereas the vertex center is the barycenter of the vertices.

The use of these two cell centers is tested on the grid shown in Fig. 10.b for the solution (3.3) in a homogeneous medium. Since the grid is rough, the two different cell centers may deviate significantly.

As seen in Fig. 12, the convergence order is the same for both cases, but the normal-velocity error is smaller when using the vertex center compared to the use of the area center. In the following we therefore use the vertex center in all test runs.

Test runs on the different grids of Fig. 10 with the solution (3.3) are now performed. The convergence for the discretization in physical space is considered for these cases. As seen from Fig. 13.a, the convergence is second order for the pressure for the skew grid in Fig. 10.a, the uniform

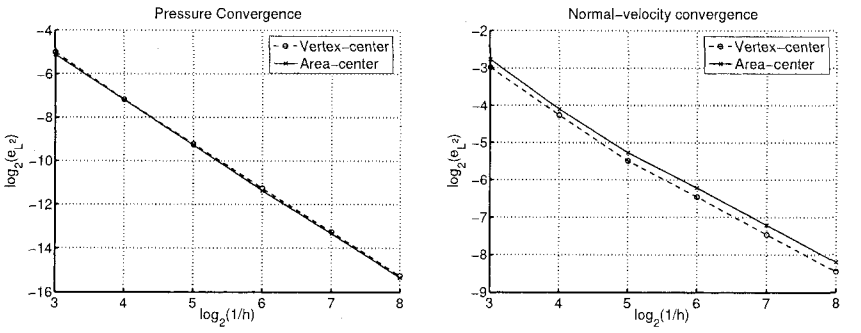

FIG. 12. *Test on cell center location with solution* (3.3) *on the grid in Fig. 10.b. Left (a): Pressure. Right (b): Edge normal velocities.*

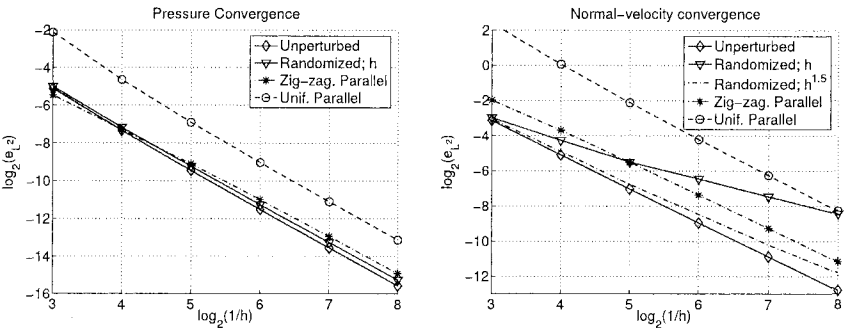

FIG. 13. *Convergence behavior for the solution* (3.3). *Left (a): Pressure. Right (b): Edge normal velocities.*

parallelogram grid, and the zig-zag parallelogram grid in Fig. 10.c. The velocity convergence is second order for both the parallelogram grids and the skew grid. Note that the domain of the uniform parallelogram grid is different from the domain in the other test cases. Therefore, only the order, and not the magnitude of the error, may be compared.

Figure 13 also shows the solutions on the rough grids shown in Fig. 10.b. For a random h^1 perturbation, the pressure is still seen to converge as h^2, whereas the convergence rate for the velocities gradually decreases to h^1, although almost $h^{1.5}$ is observed in the first refinement levels. If the perturbation is of order h^2, the velocity convergence is again of order h^2. Various h^β perturbations have been tested for $1 \leq \beta \leq 2$, and the specific case $\beta = 1.5$ is plotted in Fig. 13.b. Convergence of order $h^{1.75}$ is observed in the latest refinement step here.

Next, we compare the symmetrized version with the unsymmetric version, i.e., we compare the use of associated parallelograms with the use of

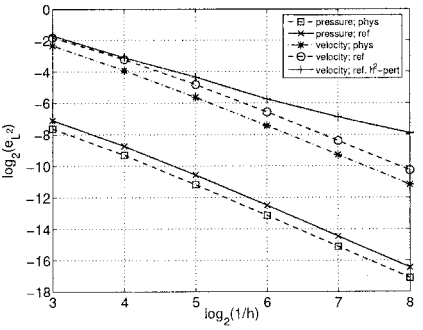

FIG. 14. *Convergence behavior of pressure and edge normal velocities for the piecewise quadratic solution* (3.7) *on the grid in Fig. 10.d.*

the physical quadrilaterals. Use of associated parallelograms may also be referred to as calculation in a reference space, since this method is identical to the method achieved by using the bilinear mapping of Sec. 2.2.

The example uses a reference solution which is a piecewise quadratic pressure, taken from [8] for a case where the medium is layered. The domain is $[0,1] \times [0,1]$, and the discontinuity line follows $x = 1/2$. Conductivities of the medium are specified by

$$\boldsymbol{K}_l = \begin{bmatrix} 50 & 0 \\ 0 & 1 \end{bmatrix}, \qquad \boldsymbol{K}_r = \begin{bmatrix} 1 & 0 \\ 0 & 10 \end{bmatrix}, \tag{3.6}$$

for which the following analytical solution holds

$$u(x,y) = \begin{cases} c_l x^2 + d_l y^2, & x < 1/2, \\ a_r + b_r x + c_r x^2 + d_r y^2, & x > 1/2. \end{cases} \tag{3.7}$$

The coefficients of (3.7) are comprised of the defined conductivities [8].

This case is simulated on the grid in Fig. 10.d, and the results are shown in Fig. 14. The asymptotic order of convergence again seems to be h^2 for both the pressure and normal velocities in physical space (the normal velocities converge as $h^{1.9}$ in the last refinement level). The order of convergence seems to be h^2 in the limit for both the pressure and normal velocities in computational space for an unperturbed grid, but initial errors are larger for the computational space discretization. When h^2-order perturbations are introduced for the corners of the grid, we see that the convergence of the normal velocities decreases to h^1, whereas h^2-order convergence is retained for the pressure. The velocity convergence in physical space is still close to h^2, and the curve will here almost coincide with the curve for the unperturbed grid. Increasing the perturbations to order h^1, our tests show that the pressure may converge slower than h^1, whereas the velocities may not even converge. For discretization in physical space, the